ACADÉMIE
DES SCIENCES
INSTITUT DE FRANCE

Comptes Rendus

Mécanique

Gwenaël Pagé, Jérémie Bettoni, Olivier Balédent and Anne-Virginie Salsac

Blood flow visualization and quantification in the carotid vascular tree by phase contrast MRI

Volume 354 (2026), p. 35-52

https://doi.org/10.5802/crmeca.320

CENTRE
MERSENNE
The Comptes Rendus. Mécanique *are a member of the*
Mersenne Center for open scientific publishing
www.centre-mersenne.org — e-ISSN : 1873-7234

ACADÉMIE
DES SCIENCES
INSTITUT DE FRANCE

Comptes Rendus. Mécanique
2026, Vol. 354, p. 35-52
`https://doi.org/10.5802/crmeca.320`

Research article

Blood flow visualization and quantification in the carotid vascular tree by phase contrast MRI

Gwenaël Pagé [a], **Jérémie Bettoni** [a], **Olivier Balédent** [a] and **Anne-Virginie Salsac** [*, b]

[a] Chimère Laboratory, University Hospital of Amiens-Picardie, Amiens, France

[b] Biomechanics and Bioengineering Laboratory (UMR 7338), Université de Technologie de Compiègne - CNRS, 60203 Compiègne, France

E-mail: a.salsac@utc.fr (A.-V. Salsac)

Abstract.

Purpose. The objective is to build a phase contrast (PC) MRI protocol, consistent with clinical practice, to provide a 3D blood flow visualization and quantification of hemodynamic parameters in the complete carotid vascular tree.
Methods. The protocol composed of 2D and 4D PC-MRI sequences was applied on 6 volunteers and then on one patient diagnosed with facial cancer to prove the feasibility of clinical translation. The vessel geometry was reconstructed from the 4D sequences and the hemodynamic parameters quantified in the common, internal and external carotids and in the facial artery. Wall shear stresses (WSS) were quantified from the 2D PC-MRI sequences to benefit from their higher resolution.
Results. Time evolution of the three-dimensional blood flow velocity and vorticity fields was successfully obtained in all the branches of the carotid vascular tree despite the large range of sizes. Consistent maps of blood flow distribution were provided by normalizing the local blood flows by that of the common carotid artery. They indicated that 72.4% (±3.9%) of blood flows into the internal carotid. WSS is higher in the internal (0.95 Pa at peak systole) than in the external carotid (0.53 Pa) and facial artery (0.15 Pa).
Conclusion. A PC-MRI protocol, applicable to patients, was designed to quantify hemodynamic parameters in vessels ranging from a few millimeters to the centimeter in diameter. It provided a complete characterization of the hemodynamic condition evolution along the carotid vascular tree, and reference values to be compared to in case of pathology.

Keywords. Blood flow, MRI, Phase contrast, Carotid, Wall shear stress.

Manuscript received 15 April 2025, accepted 12 August 2025, online since 28 January 2026.

1. Introduction

It has been well established that disturbed flow and hemodynamic forces impact vascular endothelium promoting atherosclerosis [1,2]. One prime location where the correlation between disturbed flow and atherosclerotic lesions was early revealed is carotid bifurcation [3,4]. It was shown how shear stress variations from baseline values affect vascular homeostasis [5] and the role that they play in mechanotransduction phenomena within endothelial cells [6]. Assessment of the blood flow conditions in the carotids is thus necessary to prevent and treat diseases [7]. However, most studies focused on the internal carotid artery [8,9], so that the hemodynamics in

---

[*] Corresponding author

the external carotid artery and its downstream bifurcations still remain poorly documented. This limits the understanding of hemodynamic distribution within the carotid vascular tree, which negatively impacts the treatment of head and neck pathologies like arterio-venous malformations and stenoses [10,11], as well as cancer surgery, radiation therapy and vascular embolization [12,13]. There is thus a need for a non-invasive imaging protocol capable of visualizing the entire carotid vascular tree, of quantifying the blood flow velocity field within it and of accurately estimating the biomechanical parameters associated with hemodynamics (e.g. the Wall Shear Stress (WSS) and Oscillatory Shear Index (OSI)).

Several methods are currently available to assess blood flow velocities in carotid bifurcation, such as Doppler ultrasound or Phase Contrast Magnetic Resonance Imaging (PC-MRI) [14–17]. The 2D PC-MRI method has the advantage over Doppler ultrasound to provide an accurate mapping of the velocity field distribution, from which one can compute the WSS and OSI parameters [18,19]. We showed the feasibility of using 2D PC-MRI to image the entire external carotid vascular tree and quantify the blood velocity fields in its downstream vessels that are less than 5 mm in diameter [20,21]. In the past decade, the advent of 4D PC-MRI has provided a novel approach for volumetric assessment of vascular structures, incorporating encoding of the three spatial dimensions. This advancement enables enhanced visualization and comprehensive analysis of blood flow dynamics within arterial networks. But currently, 4D PC-MRI has long acquisition times and is mostly applied in clinical routine to large vessels such as the aorta [22], where the diameter is above or close to 1 cm [23,24]. Still, several research studies applied 4D PC-MRI to intracranial arteries [25,26] or investigated hemodynamic conditions in vitro, for instance within giant intracranial aneurysms [23]. They showed the ability of 4D PC-MRI to provide three-dimensional (3D) visualization of physiological and pathological flow patterns [27,28] and the interest in having the full 3D velocity field to compute the WSS distribution [8]. However, the spatial resolution indicated in previous studies is too limited to assess blood flow hemodynamics with sufficient accuracy in these vessels, and hence the WSS.

Development of acceleration factors for 4D PC-MRI sequences enabled to improve spatial resolution and opened the possibility of exploring millimetric vessels in the carotid vascular tree [28,29]. We demonstrated the feasibility of applying 4D PC-MRI on vessel phantoms and volunteers to quantify the mean and peak velocities in vessels less than 5 mm in diameter [30]. High accuracy measurements were obtained thanks to the use of a surface coil, which is not compatible with clinical practice as quantification of the right and left arteries is necessary. It is the objective of this study to generalize the method in order to allow for blood flow quantification in both carotid vascular trees in a same acquisition, and to assess the three components of the velocity vector in order to estimate other biomechanical quantities. Blood flow pattern, vorticity field, WSS and OSI have only been determined in the common and internal carotid arteries [22,27,31] and recently in the external carotid [32] but to our knowledge these parameters have never been determined in its downstream branches. A full biomechanical characterization in the carotid vascular tree will help diagnose pathological flow conditions, but one limitation is the spatial resolution of 4D PC-MRI [18]. The establishment of a comprehensive protocol for quantifying hemodynamic parameters in both the carotid arteries and smaller arteries like the facial artery would yield valuable insights for diagnosing diverse maxillofacial pathologies. Furthermore, such a protocol would assist surgeons in identifying the most suitable artery for flap connection during partial facial graft procedures.

The purpose of this study is to develop a flow MRI protocol consistent with clinical practice to provide a volumetric visualization of the full carotid vascular tree and a quantitative assessment of the blow flow parameters in vessels of diameters less than 5 mm. The protocol, composed of 2D and 4D PC-MRI sequences, is applied to the Common Carotid Artery (CCA), Internal Carotid Artery (ICA), External Carotid Artery (ECA) and Facial Artery (FA). To validate the developed protocol and show its pertinence within a clinical context, we apply it to a patient with a cancerous tumour located in the right intermaxillary region. The objective is to assess the impact of the tumor on the local hemodynamics and quantify the blood flow rates ahead of the tumor resection surgery. It is indeed a case where reconstructive surgery is required upon resection. We show the benefit of having access during the planning of the surgery to hemodynamic information besides morphological ones, in order to determine which recipient vessels to use to connect the vessels of the graft.

2. Methods

2.1. *Population*

Six healthy volunteers (five women, one man) of age 22.2 ± 1.6 years were recruited, as well as one patient in order to prove the applicability of the imaging method to patients and its potential to provide hemodynamic information in physiological and pathological cases. The patient had been diagnosed with a squamous carcinoma located in the right intermaxillary region. In vivo data acquisitions were conducted following the approval by the local ethics committee (No. 2013-A00319-39) registered in clinicaltrail.gov (No. NCT02829190) and were performed in accordance with the ethical standards of the 1964 Declaration of Helsinki. Written informed consent was obtained from all the participants.

2.2. *MR acquisitions*

The anatomical and functional acquisitions of the carotid vascular tree were performed on a 3T research MR scanner (Achieva dStream, Philips, Netherlands) with 32 channel dS Head coil. The vessel geometry was first obtained with a 3D Time-Of-Flight (TOF) sequence and used to decide where to position the 2D slices and 3D volume in which to apply the PC-MRI sequences (Figure 1). The 3D TOF was acquired with the following parameters: FOV = 200 × 200 mm^2, TE/TR = 3/23 ms, spatial resolution = 0.6 × 0.6 × 2 mm^3, scanning time ∼ 5 min. The number of slices was set depending on the carotid bifurcation size.

For the evaluation of hemodynamics, PC-MRI sequences were employed. Wall-motion artifacts were minimized by prospective electrocardiography gating. The three-dimensional velocity fields were acquired with 4D PC-MRI sequences. The right and left carotid vascular trees were acquired in a same 4D PC-MRI volume (blue dotted box in Figure 1). A k-t PCA method was applied to reduce the acquisition time. The k-t PCA reconstruction, developed by Gyrotools LLC (Zurich, Switzerland), was set at 4 to limit the influence of the k-t PCA acceleration factor on the flow measurements as previously described [30]. Data were acquired in an axial volume and the parameters of the 4D PC-MRI were as follows: FOV = 120 × 120 mm^2, TE/TR = 7/12 ms, spatial resolution = 0.8 × 0.8 × 0.8 mm^3, k-t PCA acceleration factor = 4, number of slices = 40, encoding velocity = 70 cm·s^{-1}, 16 frames for each cardiac cycle, acquisition time of approximately 9 min depending on the heart rate.

To complete the study, 2D PC-MRI acquisitions were performed with a higher spatial resolution than for the 4D PC-MRI ones. A first acquisition was taken in a plane cutting the ICA and ECA perpendicularly to their axis and a second one in a plane perpendicular to the FA. The planes were respectively shown in green and orange in Figure 1. The 2D PC-MRI sequences were acquired with the following parameters: FOV = 120 × 120 mm^2, TE/TR = 7/12 ms, spatial resolution = 0.25 × 0.25 × 2 mm^3, SENSE = 2, 32 frames for each cardiac cycle, scanning time ∼2 min. The right and left ICA and ECA were quantified with an encoding velocity v_{enc} = 80 cm·s^{-1} within the same slice. The right and left FA were imaged in their descending portion after the bifurcation with the ECA, using an encoding velocity v_{enc} = 35 cm·s^{-1}.

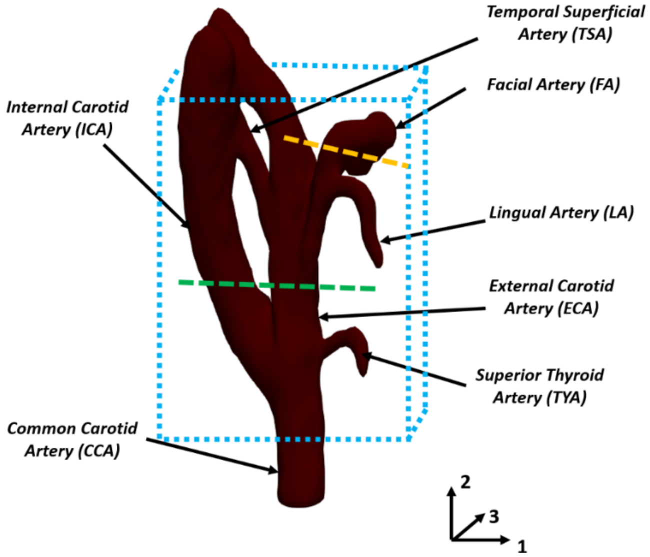

Figure 1. Geometry of the carotid vascular tree (shown for the reference case). 2D PC-MRI is acquired in the green and orange planes to image the internal and the external carotid arteries and the facial artery, respectively. The 4D PC-MRI is acquired in the dotted blue box. Directions 1, 2 and 3 are oriented along the MR Anterior–Posterior (AP), Feet-Head (FH) and Right–Left (RL) directions, respectively.

2.3. *Post-processing*

2.3.1. *Geometry reconstruction of the carotid vascular tree from 3D TOF images*

To reconstruct the geometry of the carotid vascular tree, the 3D TOF images were imported into the ITK-SNAP software [33]. The 3D geodesic active contour method, developed by Caselles et al. [34] and implemented in the software, was applied to the different segments of the vessels. Figure 2 shows the geometry of the right carotid vascular tree for each volunteer.

2.3.2. *Post-processing of 4D PC-MRI sequences*

The blood velocity data acquired for each subject using 4D PC-MRI were post-processed using homemade software developed in an Interactive Data Language environment (ITT, Visual Information Solutions, Boulder, Colorado). The data consist of magnitude and phase images contained in the DICOM images. From the phase images, the velocity components $v_1(t)$, $v_2(t)$ and $v_3(t)$ were extracted, expressed at each time t, in the coordinate system shown in Figure 1. It should be noted that data analysis incorporated corrections for velocity aliasing. The corresponding velocity magnitude $\|\vec{v}\|$ was computed as $\|\vec{v}(t)\|^2 = \sum_{i=1}^{3} v_i(t)^2$ at each voxel. A Fast Fourier Transform was applied to each velocity magnitude voxel in order to segment the vessels over time. Indeed, the voxels located within the vessels were characterized by a cyclic pulsatile flow and could be distinguished on the frequency Fourier spectrum from those corresponding to the surrounding tissues, which displayed quasi-immobility. The segmentation process relied on a threshold criterion applied to the frequency Fourier spectrum to select the voxels having a frequency close to the cardiac frequency [35]. For each voxel, a rapid Fourier transform was subsequently employed to acquire the Fourier spectrum of the temporal signal. Based on the applied threshold, the voxel was categorized as either noise or a vessel. This procedure was executed for each slice within the 4D flow dataset to reconstruct the three-dimensional morphology of the vessels. A slice was subsequently positioned on the numerical

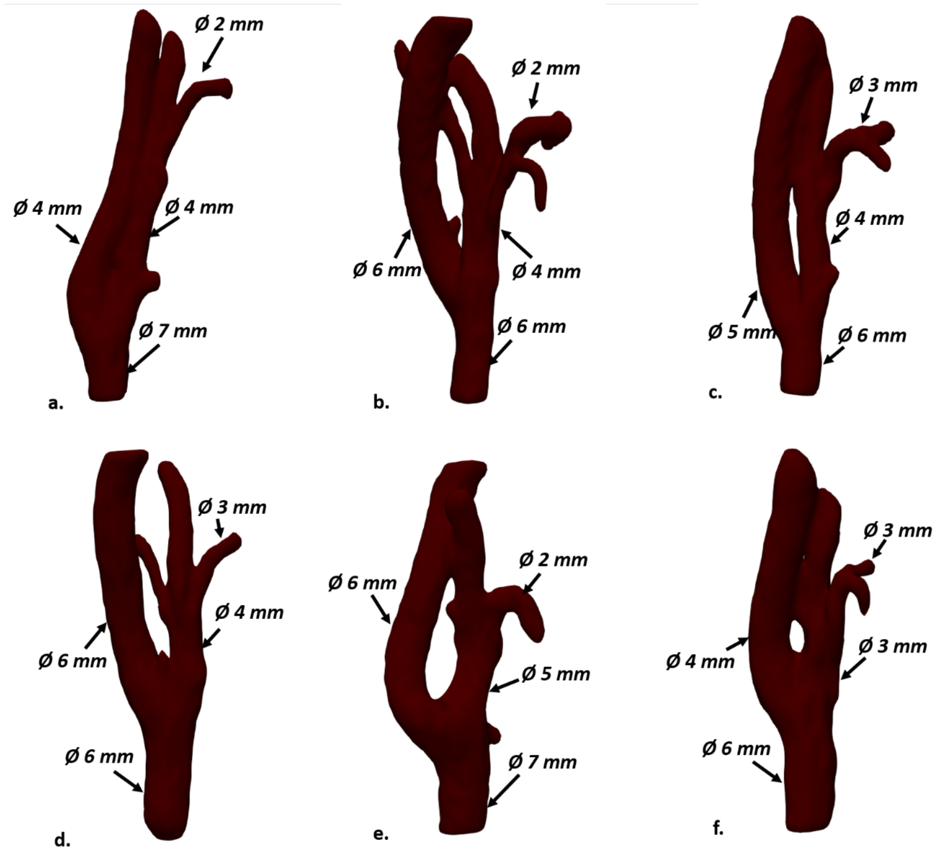

Figure 2. Right carotid bifurcation geometry of each of the six volunteers, reconstructed from 3D TOF images with the ITK-SNAP software. The vascular geometry shown in (d) will be used as a reference case.

volume to perpendicularly segment the examined vessel, enabling quantification of the blood flow rate and blood flow velocities within the segmented vessel.

To visualize the velocity field and analyze the blood flow distribution in the carotid vascular tree, the velocity components $v_1(t)$, $v_2(t)$ and $v_3(t)$ were exported to Paraview software (Kitware, USA). The vorticity vector $\vec{\omega}$ was calculated according to $\vec{\omega} = \nabla \times \vec{v}(i_1, i_2, i_3)$. In the subsequent analysis, the focus was placed on the flow data at peak systole and peak diastole.

2.3.3. *2D PC-MRI post-processing*

The 3D velocity field was additionally measured with 2D PC-MRI within different planes cutting the ICA, ECA and FA vessels perpendicularly to their axis (Figure 1). The Gradient Vector Flow method [36] was used to determine the vessel boundaries through active contour segmentation. Figure 3 shows an example of the active contour applied to the FA. Briefly, a contour C was placed on the magnitude images and defined as a closed parametric curve $c(s) = [x(s), y(s)]$, where $s \in [0,1]$ was the curvilinear abscissa. On the active contour, the energy function was computed as

$$E = \int_0^1 \frac{1}{2}(\alpha|c'(s)|^2 + \beta|c''(s)|^2) + E_{\text{ext}}(c(s))\,\mathrm{d}s, \qquad (1)$$

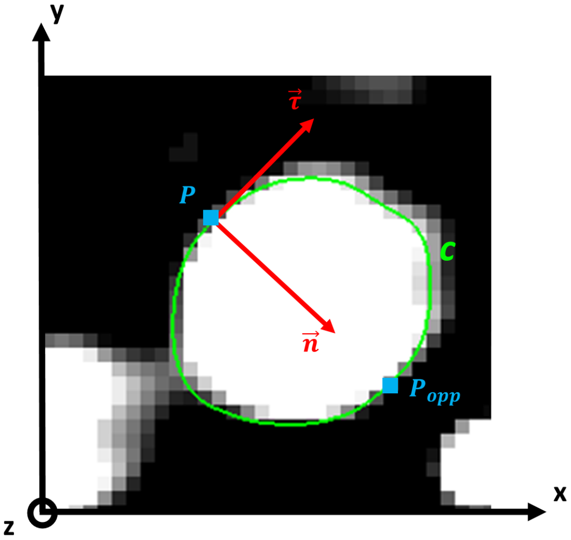

Figure 3. Contour (C) of the facial artery after the application of the active contour algorithm.

where α and β were the weighting parameters controlling the active contour tension and rigidity, respectively. The first two terms on the right-hand side of the Equation (1) represented the internal energy along the contour. The third term was the external energy typically defined as the local features of the image $\mathrm{I}(x, y)$, $E_{\text{ext}} = -|\nabla \mathrm{I}(x, y)|^2$. The minimization of the energy function had to satisfy the Euler equation

$$\alpha c''(s) - \beta c''''(s) - \nabla E_{\text{ext}} = 0, \tag{2}$$

which indicated that, at equilibrium, the contour satisfied the force balance $F_{\text{int}} + F_{\text{ext}} = 0$, where $F_{\text{int}} = \alpha c''(s) - \beta c''''(s)$ and $F_{\text{ext}} = -\nabla E_{\text{ext}}$. In the case of a static external force, the equilibrium solution was found by solving

$$c_t(s, t) = \alpha c''(s, t) - \beta c''''(s, t) - \vartheta(x, y), \tag{3}$$

where $\vartheta(x, y)$ was called the gradient vector flow force field.

To compute the gradient vector flow, an edge map $f(x, y)$ was derived from the original image $\mathrm{I}(x, y)$. For grayscale or binary images, the edge map could be expressed as $f(x, y) = E_{\text{ext}}(x, y)$. The gradient vector flow refered to vector fields obtained by propagating the gradient vector of the edge map. The gradient vector flow force field $\vartheta(x, y)$ was found by minimizing the energy function

$$\varepsilon = \iint \gamma \nabla^2 \vartheta(x, y) + |\nabla f|^2 |\vartheta(x, y) - \nabla f|^2 \, \mathrm{d}x \, \mathrm{d}y. \tag{4}$$

Compared with the traditional snake model defined in (1), the gradient vector flow snake had the ability to broaden the catching range of the initial contour and of high curvature regions in the object contour. The weighting parameter γ was a regularization parameter, that increased with the amount of noise.

The gradient vector flow snake method was applied to the ICA, ECA and FA. Knowing their cross-section S, the equivalent diameter of the arteries was calculated as $(S/\pi)^{1/2}$.

2.3.4. *Flow rate quantification*

The flow rate was quantified in the ICA, ECA and FA from the velocity magnitude $\|\vec{v}\|$ in the case of the 4D PC-MRI sequences and from the velocity component encoded along the z direction

(Figure 3) for the 2D PC-MRI sequences, by discrete integration over the reconstructed cross-sections. Corrections for velocity aliasing and background phase errors were applied [37]. The time-averaged flow rate Q was deduced by integration over one cardiac cycle.

2.3.5. *WSS calculation based on 2D PC-MRI images*

The WSS in the ICA, ECA and FA were calculated using Matlab (Matlab 2015a, The MathWorks, Massachusetts, USA) from 2D PC-MRI data only. The spatial resolution of 4D PC-MRI ($0.8 \times 0.8\ \text{mm}^2$) was indeed insufficient to get good accuracy for the vessels downstream of the external carotid artery, since there were less than 10 pixels along the diameter. The contour C was discretized with points separated by one pixel. Let $P(x_P, y_P)$ be one point of the contour C. The algorithm to compute the WSS at point P was detailed in the Appendix.

The OSI was deduced following the method proposed by Ku et al. [3]

$$\text{OSI} = \frac{1}{2}\left(1 - \frac{\left|\int_0^T \text{WSS}\,\mathrm{d}t\right|}{\int_0^T |\text{WSS}|\,\mathrm{d}t}\right), \tag{5}$$

where T denoted the period of the cardiac cycle.

2.3.6. *WSS calculation based on 4D PC-MRI images*

To compute the WSS from 4D PC-MRI images, a similar method as proposed by Stalder et al. was applied [18]. The three velocities volume encoded in each spatial direction were extracted from the numerical provided by the 4D post-processing method. A cubic B-spline function was employed to approximate the discrete velocity measurements obtained from a velocity profile. This profile extended along a line passing through the centroid of the boundary and imposed a zero-velocity condition on the wall. The derivative of the B-spline function with respect to the radial direction was multiplying by the blood dynamic viscosity to estimate the WSS. Finally, WSS values were spatially averaged and estimated for each time frame.

2.4. *Statistical analysis*

The blood flow distribution within the carotid vascular tree was calculated using the flow rate ratio Q^*_k

$$Q^*_k = \frac{Q_k}{Q_{\text{CCA}}}$$

where Q_k was the time-average flow rate in artery k (with k = ICA, ECA and FA) and Q_{CCA} was the time-average flow rate in the common carotid artery CCA. Results were reported as mean with standard deviation. Statistical analysis to compare the flow rate ratio and the WSS in different arteries was performed using a non-parametric Mann–Whitney test with GraphPad (GraphPad Prism v. 7.00 for Windows, GraphPad software, San Diego, CA).

3. Results

3.1. *Anatomy of the carotid vascular tree*

Among the 6 volunteers, the mean diameters of the sequenced arteries are $d_{\text{CCA}} = 6.7 \pm 0.6$ mm for CCA, $d_{\text{ICA}} = 5.3 \pm 0.6$ mm for ICA, $d_{\text{ECA}} = 4.2 \pm 0.7$ mm for ECA and d_{FA} 2.5 ± 0.5 mm for FA. When non-dimensionalizing the diameters of each patient with that of the corresponding common carotid artery CCA, we find that the mean normalized diameters are equal to $d_{\text{ICA}}/d_{\text{CCA}} = 0.8 \pm 0.1$, $d_{\text{ECA}}/d_{\text{CCA}} = 0.6 \pm 0.1$, $d_{\text{FA}}/d_{\text{CCA}} = 0.4 \pm 0.1$.

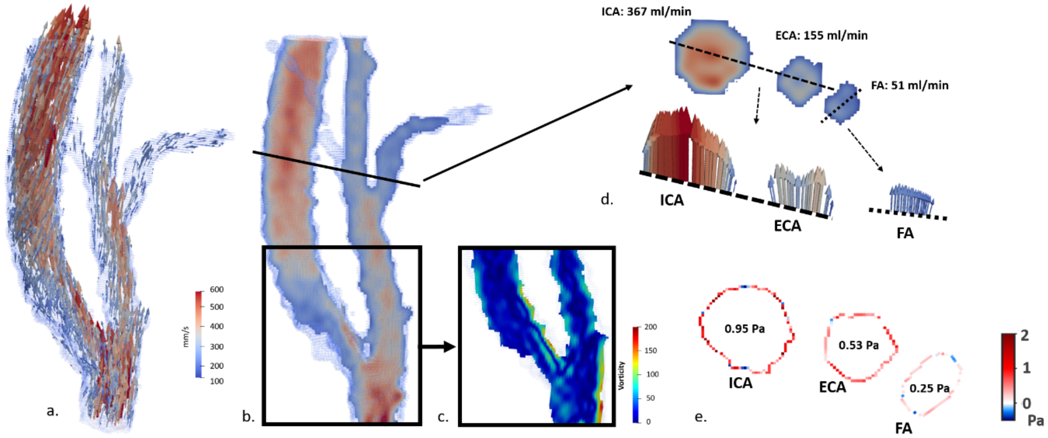

Figure 4. Flow data measured at peak systole in the right carotid bifurcation for the reference case. (a) Velocity vectors reconstructed from the 4D PC-MRI sequence. (b) Velocity field displayed in the longitudinal plane of the vascular tree. (c) Vorticity field in the carotid bifurcation region. (d) Velocity field in the internal and external carotid arteries (ICA and ECA, respectively) and facial artery (FA) measured in the green cutting plane. The velocity vectors are represented along a central line (red for ICA and ECA and yellow for FA). The systolic flow rates are displayed for each vessel. (e) Wall shear stress map and space-average value measured for the ICA, ECA and FA from the 2D PC-MRI acquisitions.

We chose Volunteer 2 (Figure 2b) as the reference case to detail the general features of hemodynamics in the carotid tree, as it has the most common anatomical variation of the carotid vascular tree and its time-averaged flow rate is consistent with values of the literature for healthy people [16,20,21].

3.2. *Flow distribution and hemodynamic stresses in the carotid branches*

The flow data are represented in Figures 4 and 5 at peak systole and diastole, respectively. The velocity fields show a non-uniform velocity distribution within the vascular tree, with higher velocity magnitudes in the ICA than in the ECA both at peak systole (Figure 4a) and diastole (Figure 5a). To enhance the identification of blood flow distribution, the magnitude of the velocity vector was visualized within a cross-sectional view of the vessels (Figures 4b and 5b). An increase in velocity magnitude was observed on both sides of the bifurcation at the beginning of the ECA and ICA. The vessels stemming from the ECA are also characterized by much reduced velocity magnitudes, the flow rate in the facial artery being for instance 7 and 80 times smaller than in the ICA at peak systole (Figure 4d) and diastole (Figure 5d), respectively. The vorticity fields (Figures 4c and 5c) show no net recirculation region in the carotid bulb but highlight velocity gradients along the walls. They could be overestimated due to the resolution of the 4D PC-MRI measurement, which is too low for vessels of such small sizes and justifies why we have not calculated the WSS from these data sets.

More information on the velocity distribution is provided by the velocity vectors of Figures 4d and 5d. Flow profiles measured from 2D and 4D PC-MRI are similar as observed in Figure 6. The difference between flow profiles seem to be more important for the FA which has a smaller diameter than carotid arteries. Flow profiles are then less accurate in 4D PC-MRI where the resolution is lower than 2D PC-MRI sequence.The pulsatility of the flow makes the velocity profiles be rather flat as predicted by Womersley [38]. Thin boundary layers are especially observed in the ECA and FA. A more parabolic flow profile is observed in the ICA. It must be

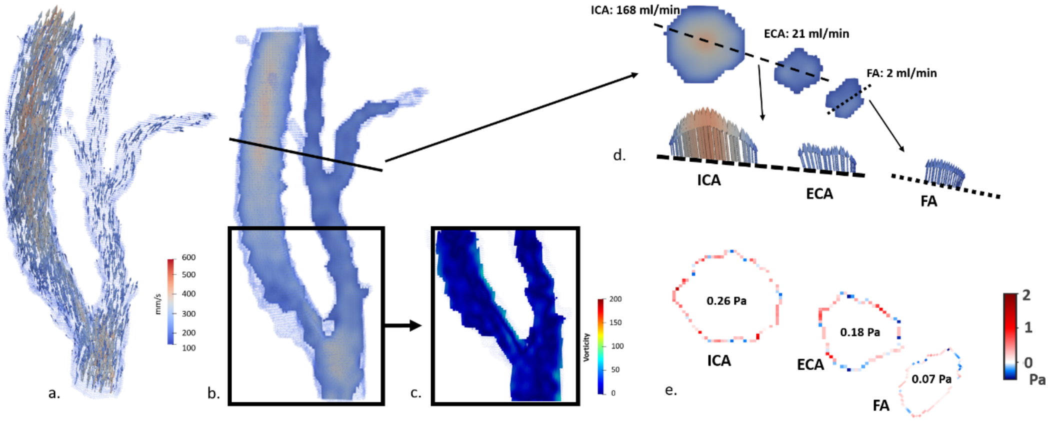

Figure 5. Flow data measured at peak diastole in the right carotid bifurcation for the reference case. (a) Velocity vectors reconstructed from the 4D PC-MRI sequence. (b) Velocity field displayed in the longitudinal plane of the vascular tree. (c) Vorticity field in the carotid bifurcation region. (d) Velocity field in the internal and external carotid arteries (ICA and ECA, respectively) and facial artery (FA) measured in the green cutting plane. The velocity vectors are represented along a central line (red for ICA and ECA and yellow for FA). The diastolic flow rates are displayed for each vessel. (e) Wall shear stress map and space-average value measured for the ICA, ECA and FA from the 2D PC-MRI acquisitions.

linked to the fact that the blood flow at peak diastole is only reduced to half its systolic value, which must aim at maintaining brain vascularization as constant as possible.

Figures 4d and 5d showed that the blood flow rate is higher in the ICA than in the ECA and FA both at peak systole and diastole. To further investigate this effect, the dimensional and normalized flow rates, measured in the green cutting plane (see Figures 4–5) in the right and left carotid vascular trees of the six volunteers, are represented in Figure 7. The mean values of flow rate are 266.6 ± 39.4 ml/min in the ICA, 100.5 ± 20.2 ml/min in the ECA and 21.6 ± 9.6 ml/min in the FA (Figure 7a). The time-averaged flow rate is significantly higher in the ICA than in the ECA ($p = 0.0158$) and the FA ($p < 0.0001$).

Non-dimensionalizing the values of each patient by the corresponding flow rate in the CCA allows us to reduce the variability of the measurements as shown in Figure 7b. It thus provides general information on blood flow distribution in the carotid vascular tree in the healthy population. We find that blood flow goes mainly in the ICA ($72.4 \pm 3.9\%$) rather than the ECA ($27.6 \pm 4.3\%$), and that the FA represents only a small portion ($6.2 \pm 3.4\%$) of the total blood flow.

Figures 4e and 5e provided first information on the WSS amplitude and distribution for the volunteer chosen as a reference case. The time- and space-averaged values of WSS show, that, similarly to the blood flow rate, the WSS is higher in the ICA (e.g. 0.95 Pa at peak systole) than in the ECA (0.53 Pa) and FA (0.15 Pa). The time- and space-averaged values of WSS, calculated from the velocity measurements obtained in the right and left carotid vascular trees of the six volunteers, are given in Figure 8. The mean WSS is 0.36 ± 0.09 N/m^2 in the ICA, 0.24 ± 0.07 N/m^2 in the ECA and 0.13 ± 0.04 N/m^2 in the FA. Significant differences in WSS are observed between ICA and the FA ($p < 0.0001$), and between ECA and FA ($p = 0.0111$), while no significative difference is found for ICA and ECA ($p = 0.1031$) when averaged over the vessel contour and cardiac period. The OSI values are similar in all the arteries of the healthy population with an averaged OSI of 0.03 ± 0.06 in the ICA, 0.04 ± 0.05 in the ECA and 0.04 ± 0.03 in the FA.

Comparative analysis was conducted between WSS values derived from 2D PC-MRI images and those obtained using 4D PC-MRI (Figure 9). The findings revealed a notable correlation between WSS measurements obtained from the two modalities ($r = 0.90, p < 0.0001$). On an

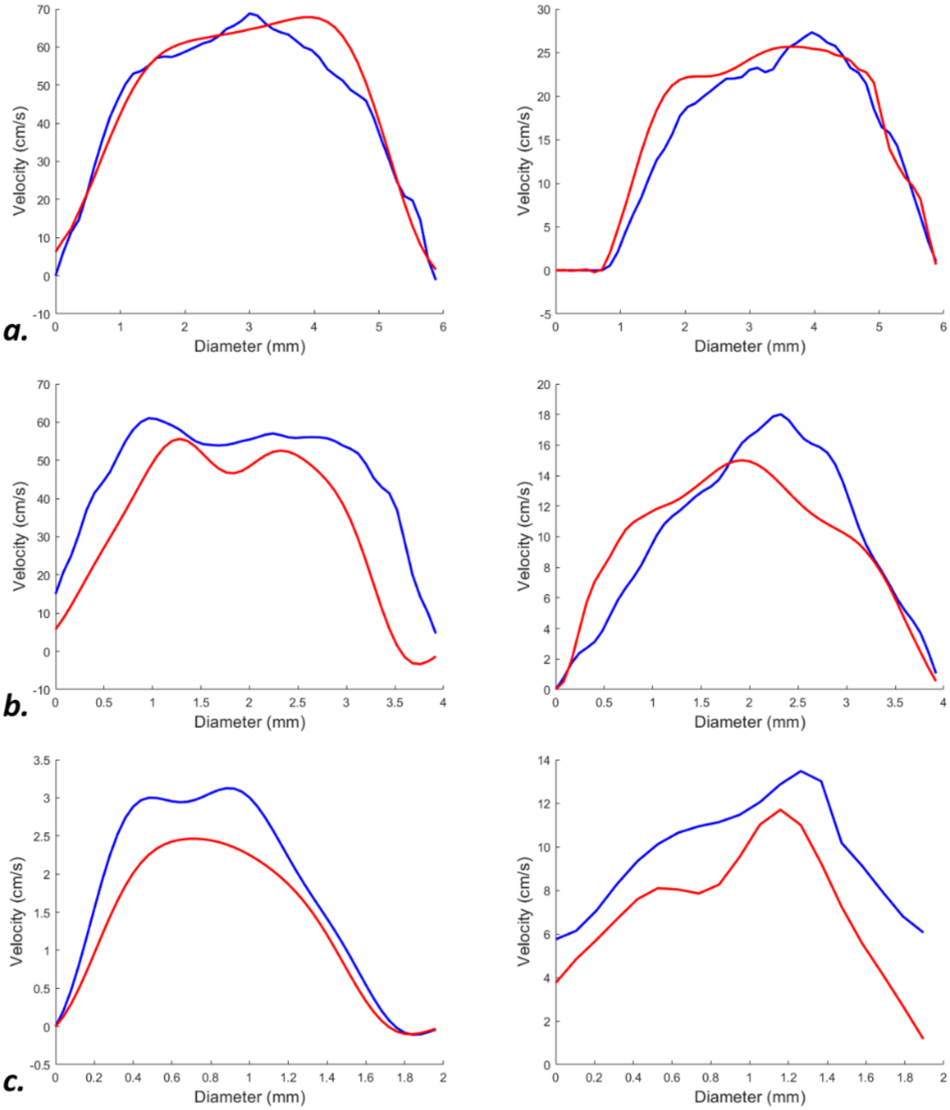

Figure 6. Flow profiles measured from 2D PC-MRI (blue) and 4D PC-MRI images (red) at systole (left column) and diastole peak (right column) in ICA (a), ECA (b) and FA (c).

individual artery basis, a favorable correlation was observed for the internal carotid artery (ICA) and external carotid artery (ECA) ($r = 0.88$, $p < 0.0002$ and $r = 0.82$, $p = 0.0012$, respectively), while a comparatively lower correlation was noted for the femoral artery (FA) ($r = 0.63, p = 0.0027$). Considering the smaller size of the FA, it is plausible that WSS estimation derived from 4D PC-MRI images may exhibit decreased accuracy compared to results obtained through 2D PC-MRI, which offers superior resolution.

3.3. *Flow distribution and hemodynamic stresses in a patient with carcinoma*

To prove the feasibility of the method to investigate the blood flow distribution in a patient, we show the flow data measured in the right carotid bifurcation of a patient with carcinoma at peak

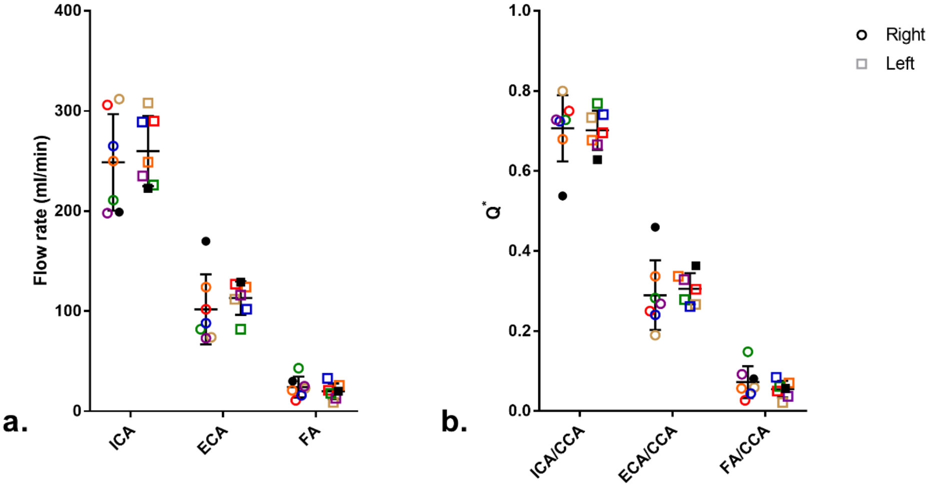

Figure 7. (a) Time-average flow rate measured in each volunteer and in the patient in the internal and external carotids (ICA and ECA, respectively) and in the facial artery (FA) of the right and left carotid trees. (b) Normalized flow rate calculated as the ratio between the time-average flow rate measured in the ICA, ECA and FA and the corresponding value in the common carotid artery (CCA). Each volunteer is displayed with an empty symbol with different colors and the patient with a full symbol.

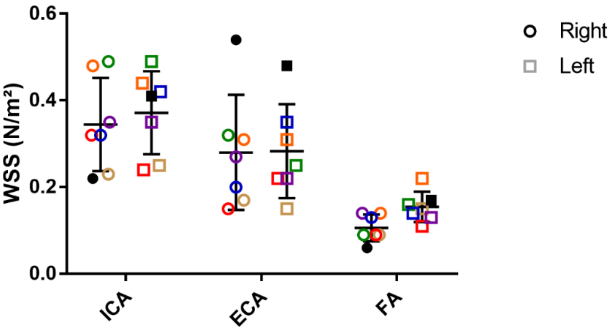

Figure 8. Time- and space-averaged wall shear stress measured in each volunteer and in the patient in the internal and external carotids (ICA and ECA, respectively) and in the facial artery (FA) of the right and left carotid trees.

systole (Figure 10) and diastole (Figure 11). It is striking how much higher the blood flow in the external carotid is as compared to the healthy reference case, which can also be seen in Figure 6. In the patient, the normalized flow rates are close to 50% for the ICA and ECA, indicating that an equivalent blood flow volume goes from the CCA to both branches. But, despite these differences, the hemodynamics in the FA seems to be similar to the flow patterns observed in the reference case.

The higher flow rate impacts the velocity field distribution across the vessel, which is equivalent to that in the external carotid (Figure 10d). Moreover, the WSS is higher in the right ECA than in the ICA, which is the opposite to what is measured in the volunteers. It is also different from the measurements in the left carotid bifurcation, where the WSS have similar values in the ECA and ICA (data not shown).

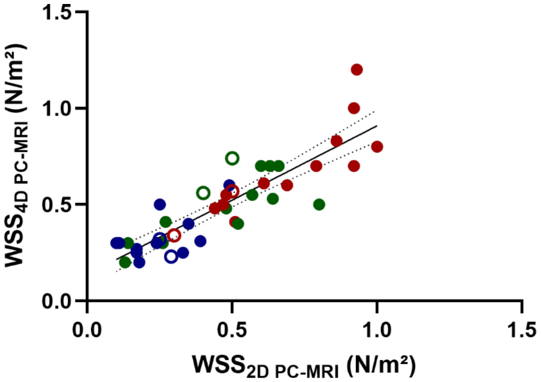

Figure 9. Correlation plot between WSS measured with 2D PC-MRI and 4D PC-MRI. The empty symbols correspond to the data measured from patient images. Red, blue and green circles represent, respectively, WSS measured in ICA, ECA and FA.

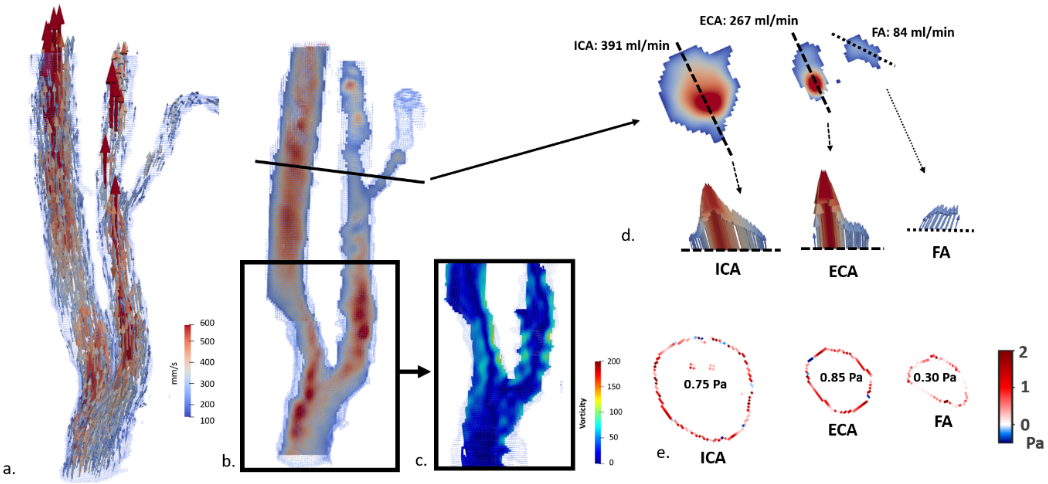

Figure 10. Flow data measured at peak systole in the right carotid bifurcation of the patient with a carcinoma in the maxillary area. (a) Velocity vectors reconstructed from the 4D PC-MRI sequence. (b) Velocity field displayed in the longitudinal plane of the vascular tree. (c) Vorticity field in the carotid bifurcation region. (d) Velocity field in the internal and external carotid arteries (ICA and ECA, respectively) and facial artery (FA) measured in the green cutting plane. The velocity vectors are represented along a central line (red for ICA and ECA and yellow for FA). The systolic flow rates are displayed for each vessel. (e) Wall shear stress map and space-average value measured for the ICA, ECA and FA from the 2D PC-MRI acquisitions.

4. Discussion

The present study proposes a PC-MRI methodology using a single sequence to characterize the hemodynamics in both the right and left carotid vascular trees, and from the Common Carotid Artery to the smaller vessels (e.g. the Facial Artery). The results confirm that the combination of 2D and 4D PC-MRI allows to quantify all the hemodynamics parameters (the velocity fields and vorticity fields, blood flow rate and blood flow distribution, WSS, WSR, . . .) in vessels ranging from a few millimeters to a centimeter in diameter. It also proves the feasibility of finding consistent hemodynamic measurements in volunteers and of applying the protocol to patients.

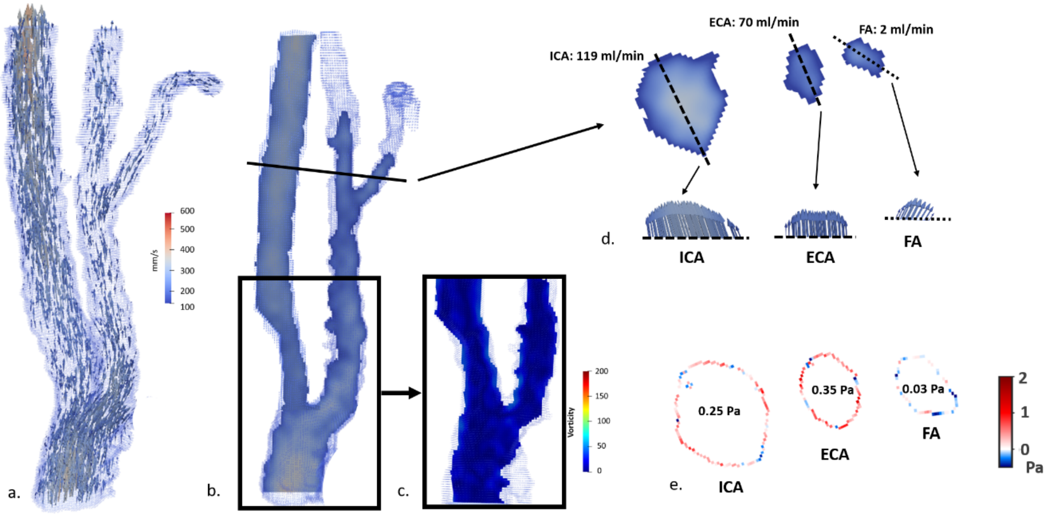

Figure 11. Flow data measured at peak diastole in the right carotid bifurcation of the patient with a carcinoma in the maxillary area. (a) Velocity vectors reconstructed from the 4D PC-MRI sequence. (b) Velocity field displayed in the longitudinal plane of the vascular tree. (c) Vorticity field in the carotid bifurcation region. (d) Velocity field in the internal and external carotid arteries (ICA and ECA, respectively) and facial artery (FA) measured in the green cutting plane. The velocity vectors are represented along a central line (red for ICA and ECA and yellow for FA). The diastolic flow rates are displayed for each vessel. (e) Wall shear stress map and space-average value measured for the ICA, ECA and FA from the 2D PC-MRI acquisitions.

The 32 head coil has a lower signal-to-noise ratio compared to the 47-mm microscopic coil, wich had been previously used to measure blood flow velocities in some vessels of the carotid bifurcation [20,30]. It also has the advantage of having a higher depth of penetration of coils, the latter being inversely proportional to the coil diameter. Using a 32 head coil thus limits the non-uniformity of the signal on the images and allows to acquiring both carotid bifurcations in the same sequence, which drastically reduces the acquisition time. Despite the loss of signal, the blood flow values provided by the 4D PC-MRI sequence compare very well with those in the literature even for vessels as small as the FA [16,20,30].

Compare to 2D PC-MRI, 4 PC-MRI provides volumetric imaging of a full vessel tree and quantitative assessment of the three-dimensional blood flow velocity fields. It is thus possible to visualize parameters such as the velocity or vorticity vector field. These hemodynamic parameters are relevant to analyze the complex blood flow patterns and diagnose carotid stenosis or atherosclerosis [39,40]. The measurement of the complete set of hemodynamic quantities could even be performed in the FA, although a single encoding velocity had been used (note that using a dual encoding velocity is at the detriment of the sequence acquisition time). Compared to the ICA and ECA, the number of pixels across the vessel is reduced due to the small diameter size, but it is sufficient for a hemodynamic analysis to be performed. We could, for instance, show that the velocity profile is in accordance with the pulsed blood flow predictions by Womersley. This kind of analysis is pertinent for clinicians to evaluate blood flow distribution across the entire imaged network or to choose recipient vessels in free-flap facial surgery [41].

The underestimation of velocity gradients along the wall in the vorticity fields (specifically when an acceleration is applied [30]) highlights the need to add a 2D PC-MRI sequence to quantify blood flow with better resolution. Indeed, to calculate parameters like the WSS or OSI, an accurate measurement of the blood velocity is required and 4D PC-MRI cannot provide such a spatial resolution at present. Adding two 2D PC-MRI sequences to image the carotid bifurcation and FA increased the scanning time, but provided valuable information. Similar

WSS and OSI values to those of the literature are found in the ICA and ECA [9,22,42], which validates the measurements. The values measured in the FA are among the first ones to be reported and provide valuable information to evaluate the success of free-flap facial surgery or progression of arterio-venous malformations post-operatively [43] or to evaluate the influence of carotid stenosis on blood flow in the distal branches [44]. Furthermore, numerous studies have demonstrated the potential of OSI as an indicator of atherosclerotic plaque evolution, with an elevated OSI being associated with the development and progression of plaque. Consistently, the OSI results obtained from the healthy population in this study were found to be lower than those observed in patients with plaque in the ICA. These findings underscore the diagnostic and patient follow-up potential of the proposed protocol in cases of cardiovascular pathologies affecting carotid bifurcation.

In the context of 4D flow MRI, the visualization of blood flow provides qualitative information on vorticity, presenting a promising approach for the diagnosis of cardiovascular pathologies. Previous studies utilizing PC-MRI have primarily focused on examining vorticities in the heart and aorta [45,46]. However, investigations employing particle image velocimetry or ultrasound have indicated the potential value of assessing vorticities in carotid bifurcation [47,48]. Consistent with the findings presented in this study, it has been demonstrated that while the CCA exhibits laminar flow, the carotid bulb displays a complex flow pattern [49]. The presence of a stable vortex is crucial for maintaining blood pressure regulation. In this study involving volunteers, vorticities was predominantly observed in the carotid bulb. Nevertheless, the evaluation of vorticities in patients could serve as a reliable biomarker for diagnosing artery aneurysms. Notably, in such cases, the visualization of blood flow reveals the presence of multiple vorticity fields along the artery. Since all the blood velocities in the carotid bifurcation are acquired in a single sequence, the blood flow rated is quantified at the same time instants and thus under the same conditions. This makes analysis of blood flow distribution fully relevant and thus has a very large added value. Consistently with the literature, we find that about 3/4 of blood coming from CCA flows into the ICA and the brain [16]. Only a small portion goes to the facial artery, which must be taken accounted for, when choosing the recipient vessels pre-operatively in case of free-flap surgery. The analysis that we performed on the patient shows an equal distribution between the ICA and ECA. Hypothesis on vessel co-option induced by the tumor can thus be formulated [50,51], and further studies should investigate the effect of facial cancer on blood flow distribution. This finding mainly highlights the importance of quantifying blood flow ratios as performed in the present study to investigate the effect of stenosis cancer or post-operative facial reconstruction.

The hemodynamic MR acquisition was performed in the patient before facial surgery. It provided confirmation of a flow within the facial artery ipsilaterally to the cancerous lesion, as well as its quantification. This allowed a pre-operative choice of the recipient artery (FA) for the microanastomosed free flap reconstruction procedure. Moreover, knowledge of the arterial topography made it possible to orient the dissection and limit the operating time to the identification of the facial artery, thus reducing the risk of vascular injury. In practice, it is recommended to identify at least 2 or even 3 potential recipient vessels to avoid emergency dissection of other vascular axes in the absence of clinically visualized flow during the arteriotomy of the initially chosen artery. Although this type of event is rare in a patient with no medical-surgical history, the contribution of flow MRI will be particularly interesting in patients undergoing multiple operations or irradiation for head and neck carcinoma, where dissection and identification of vessels are sometimes very complicated and dangerous due to the fragility of vascular structures and local tissue fibrosis.

Finally, the present study introduces a blood flow MR protocol that combines 2D and 4D PC-MRI to comprehensively assess hemodynamic parameters in both the internal and external carotid arteries, as well as the downstream branches of the external carotid artery in conjunction with the facial arteries. This approach surpasses the conventional limitation of previous investigations, which typically focus solely on the internal and external carotid arteries. Hence, in addition to the potential of flow MRI in carotid bifurcation for diagnosing cardiovascular pathologies such as atherosclerotic plaque or artery aneurysm,the acquisition of hemodynamics parameters in the maxillofacial arteries holds significant potential for evaluating vessel viability prior to microsurgical reconstruction [52]. Furthermore, this valuable information can contribute to accurate diagnosis and facilitate patient follow-up, particularly in cases involving pathologies characterized by vascular tropism, such as high-flow arteriovenous malformations [53].

The purpose of the study was to propose an acquisition methodology transferable to clinical practice, to indicate which information it could provide and to prove their relevance to a few volunteers and a patient. The weak number of measurements performed on volunteers, however, makes it difficult to observe statistical differences in the flow parameters evaluated between the different arteries. It would be interesting to extend the study to a much larger population and to compare pathological cases to a complete healthy database in the future.

Declaration of interests

The authors do not work for, advise, own shares in, or receive funds from any organization that could benefit from this article, and have declared no affiliations other than their research organizations.

Appendix

The algorithm to compute the WSS at a point $P(x_P, y_P)$ of the contour C of a vessel uses the local coordinate system $(\vec{n}, \vec{\tau})$ defined in Figure 3 and consists of seven steps:

(1) The velocity at $P(x_P, y_P)$ is set to zero.

(2) The contour C is fitted in the vicinity of point $P(x_P, y_P)$ with a cubic spline f_{contour} using the *spline* function of Matlab [54,55]

$$f_{\text{contour}}(x) = A_3(x - x_{P-j})^3 + A_2(x - x_{P-j})^2 + A_1(x - x_{P-j}), \quad j = -5 \cdots +5 \tag{6}$$

where

$$\begin{aligned} A_3 &= 2y_{P-j} - 2y_{P-j+1} + y'_{P-j} + y'_{P-j+1}, \\ A_2 &= 3y_{P-j+1} - 3y_{P-j} + y'_{P-j+1} - 2y'_{P-j}, \\ A_1 &= y'_{P-j}. \end{aligned}$$

(3) The normal vector at point P is defined as $\vec{n}(n_x; n_y)$, with $n_x = -(y_P - 1/(f'_{\text{contour}}(x_P))x_P)$ and $n_y = 1/(f'_{\text{contour}}(x_P))$.

(4) We extract the coordinates of each pixel located along the vessel diameter stemming from point P in the normal direction $\vec{n}$ and ending at point P_{opp} on the opposite side of the contour (Figure 3).

(5) Using the 2D PC-MRI images, we extract the velocity encoded on the direction z along the vessel diameter $[P\,P_{\text{opp}}]$ and fit it with a cubic spline function f_{vel}

$$f_{\text{vel}}(n) = B_1(n - n_{P-l})^3 + B_2(n - n_{P-l})^2 + B_3(n - n_{P-l}), \tag{7}$$

with

$$B_1 = 2\tau_{P-l} - \tau_{P-l+1} + \tau'_{P-l} + \tau'_{P-l+1},$$

$$B_2 = 3\tau_{P-l+1} - 3\tau_{P-l} + \tau'_{P-l+1} - 2\tau'_{P-l},$$
$$B_3 = \tau'_{P-l}.$$

The spline is calculated for $n_P \leq n_l \leq n_{P\text{opp}}$, i.e. between the point $P(n_P, \tau_P)$ and $P_{\text{opp}}(n_{P\text{opp}}, \tau_{P\text{opp}})$.

(6) The velocity gradient at point P on the wall provides the wall shear rate WSR

$$\text{WSR} = \left.\frac{\partial f_{\text{vel}}}{\partial n}\right|_{n=n_j}. \tag{8}$$

(7) Finally, the *WSS* is deduced assuming that blood viscosity μ is equal to 3.5×10^{-3} Pa·s

$$\text{WSS} = \mu\text{WSR}. \tag{9}$$

References

[1] J.-J. Chiu and S. Chien, “Effects of disturbed flow on vascular endothelium: pathophysiological basis and clinical perspectives”, *Physiol. Rev.* **91** (2011), no. 1, pp. 327–387.

[2] M. A. Gimbrone and G. García-Cardeña, “Vascular endothelium, hemodynamics, and the pathobiology of atherosclerosis”, *Cardiovasc. Pathol. Off. J. Soc. Cardiovasc. Pathol.* **22** (2013), no. 1, pp. 9–15.

[3] D. N. Ku, D. P. Giddens, C. K. Zarins and S. Glagov, “Pulsatile flow and atherosclerosis in the human carotid bifurcation. Positive correlation between plaque location and low oscillating shear stress”, *Arterioscler. Dallas Tex* **5** (1985), no. 3, pp. 293–302.

[4] C. K. Zarins, D. P. Giddens, B. K. Bharadvaj, V. S. Sottiurai, R. F. Mabon and S. Glagov, “Carotid bifurcation atherosclerosis. Quantitative correlation of plaque localization with flow velocity profiles and wall shear stress”, *Circ. Res.* **53** (1983), no. 4, pp. 502–514.

[5] A. Kamiya and T. Togawa, “Adaptive regulation of wall shear stress to flow change in the canine carotid artery”, *Am. J. Physiol.* **239** (1980), no. 1, H14–H21.

[6] J. D. Humphrey, E. R. Dufresne and M. A. Schwartz, “Mechanotransduction and extracellular matrix homeostasis”, *Nat. Rev. Mol. Cell Biol.* **15** (2014), no. 12, pp. 802–812.

[7] I. Marshall, S. Zhao, P. Papathanasopoulou, P. Hoskins and X. Y. Xu, “MRI and CFD studies of pulsatile flow in healthy and stenosed carotid bifurcation models”, *J. Biomech.* **37** (2004), no. 5, pp. 679–687.

[8] M. Markl, F. Wegent, T. Zech, et al., “In vivo wall shear stress distribution in the carotid artery effect of bifurcation geometry, internal carotid artery stenosis, and recanalization therapy”, *Circ. Cardiovasc. Imaging* **3** (2010), no. 6, pp. 647–655.

[9] S.-W. Lee, L. Antiga, J. D. Spence and D. A. Steinman, “Geometry of the carotid bifurcation predicts its exposure to disturbed flow”, *Stroke* **39** (2008), no. 8, pp. 2341–2347.

[10] C.-H. Li, B.-L. Gao, J.-W. Wang, J.-F. Liu, H. Li and S.-T. Yang, “Hemodynamic factors affecting carotid sinus atherosclerotic stenosis”, *World Neurosurg.* **121** (2019), e262–e276.

[11] A. Dell’Amore, F. Castriota, S. Calvi, D. Magnano, G. Noera and M. Lamarra, “Post-traumatic carotid-jugular arterio-venous fistula”, *Heart Lung Circ.* **18** (2009), no. 4, article no. 293.

[12] S. Shah-Becker, M. Pennock, L. Sinoway, D. Goldenberg and N. Goyal, “Baroreceptor reflex failure: review of the literature and the potential impact on patients with head and neck cancer”, *Head Neck* **39** (2017), no. 10, pp. 2135–2141.

[13] L. J. King, S. N. Hasnain, J. A. Webb, J. E. Kingston, E. A. Shafford, T. A. Lister, J. Shamash and R. H. Reznek, “Asymptomatic carotid arterial disease in young patients following neck radiation therapy for hodgkin lymphoma”, *Radiology* **213** (1999), no. 1, pp. 167–172.

[14] B. Yazici, B. Erdoğmuş and A. Tugay, “Cerebral blood flow measurements of the extracranial carotid and vertebral arteries with Doppler ultrasonography in healthy adults”, *Diagn. Interv. Radiol.* **11** (2005), no. 4, pp. 195–198.

[15] A. H. Brandt, K. L. Hansen, C. Ewertsen, et al., “A comparison study of vector velocity, spectral doppler and magnetic resonance of blood flow in the common carotid artery”, *Ultrasound Med. Biol.* **44** (2018), no. 8, pp. 1751–1761.

[16] I. Marshall, P. Papathanasopoulou and K. Wartolowska, “Carotid flow rates and flow division at the bifurcation in healthy volunteers”, *Physiol. Meas.* **25** (2004), no. 3, article no. 691.

[17] A. Harloff, T. Zech, F. Wegent, C. Strecker, C. Weiller and M. Markl, “Comparison of blood flow velocity quantification by 4D flow MR imaging with ultrasound at the carotid bifurcation”, *AJNR Am. J. Neuroradiol.* **34** (2013), no. 7, pp. 1407–1413.

[18] A. f. Stalder, M. f. Russe, A. Frydrychowicz, J. Bock, J. Hennig and M. Markl, "Quantitative 2D and 3D phase contrast MRI: optimized analysis of blood flow and vessel wall parameters", *Magn. Reson. Med.* **60** (2008), no. 5, pp. 1218–1231.

[19] P. van Ooij, W. V. Potters, A. Guédon, J. J. Schneiders, H. A. Marquering, C. B. Majoie, E. vanBavel and A. J. Nederveen, "Wall shear stress estimated with phase contrast MRI in an in vitro and in vivo intracranial aneurysm", *J. Magn. Reson. Imaging* **38** (2013), no. 4, pp. 876–884.

[20] J. Bettoni, G. Pagé, A. V. Salsac, J. M. Constans, S. Testelin, B. Devauchelle, O. Balédent and S. Dakpé, "Quantitative assessment of the flow distribution in the branches of the external carotid by non-injected flow MRI", *Dentomaxillofac. Radiol.* **47** (2018), no. 8, article no. 20180153.

[21] J. Bettoni, G. Pagé, A. V. Salsac, J. M. Constans, S. Testelin, B. Devauchelle, O. Balédent and S. Dakpé, "3T non-injected phase-contrast MRI sequences for the mapping of the external carotid branches: In vivo radio-anatomical pilot study for feasibility analysis", *J. Cranio-Maxillofac. Surg.* **46** (2018), no. 1, pp. 98–106.

[22] M. Markl, P. J. Kilner and T. Ebbers, "Comprehensive 4D velocity mapping of the heart and great vessels by cardiovascular magnetic resonance", *J. Cardiovasc. Magn. Reson. Off. J. Soc. Cardiovasc. Magn. Reson.* **13** (2011), article no. 7.

[23] M. Markl, A. Frydrychowicz, S. Kozerke, M. Hope and O. Wieben, "4D flow MRI", *J. Magn. Reson. Imaging* **36** (2012), no. 5, pp. 1015–1036.

[24] O. Amili, D. Schiavazzi, S. Moen, B. Jagadeesan, P.-F. V. de Moortele and F. Coletti, "Hemodynamics in a giant intracranial aneurysm characterized by in vitro 4D flow MRI", *PLoS One* **13** (2018), no. 1, article no. e0188323.

[25] S. Meckel, L. Leitner, L. H. Bonati, et al., "Intracranial artery velocity measurement using 4D PC MRI at 3 T: comparison with transcranial ultrasound techniques and 2D PC MRI", *Neuroradiology* **55** (2013), no. 4, pp. 389–398.

[26] A. Wåhlin, K. Ambarki, R. Birgander, O. Wieben, K. M. Johnson, J. Malm and A. Eklund, "Measuring pulsatile flow in cerebral arteries using 4D phase-contrast MR imaging", *Am. J. Neuroradiol.* **34** (2013), no. 9, pp. 1740–1745.

[27] A. Harloff, F. Albrecht, J. Spreer, et al., "3D blood flow characteristics in the carotid artery bifurcation assessed by flow-sensitive 4D MRI at 3T", *Magn. Reson. Med.* **61** (2009), no. 1, pp. 65–74.

[28] H. Pedersen, S. Kozerke, S. Ringgaard, K. Nehrke and W. Y. Kim, "k-t PCA: temporally constrained k-t BLAST reconstruction using principal component analysis", *Magn. Reson. Med.* **62** (2009), no. 3, pp. 706–716.

[29] S. Kozerke, J. Tsao, R. Razavi and P. Boesiger, "Accelerating cardiac cine 3D imaging using k-t BLAST", *Magn. Reson. Med.* **52** (2004), no. 1, pp. 19–26.

[30] G. Pagé, J. Bettoni, A.-V. Salsac and O. Balédent, "Influence of principal component analysis acceleration factor on velocity measurement in 2D and 4D PC-MRI", *Magn. Reson. Mater. Phys. Biol. Med.* **31** (2018), no. 3, pp. 469–481.

[31] A. Goddi, C. Bortolotto, I. Fiorina, M. V. Raciti, M. Fanizza, E. Turpini, G. Boffelli and F. Calliada, "High-frame rate vector flow imaging of the carotid bifurcation", *Insights Imaging* **8** (2017), no. 3, pp. 319–328.

[32] E. R. Hurd, E. Iffrig, D. Jiang, J. N. Oshinski and L. H. Timmins, "Flow-based method demonstrates improved accuracy for calculating wall shear stress in arterial flows from 4D flow MRI data", *J. Biomech.* **146** (2023), article no. 111413.

[33] P. A. Yushkevich, J. Piven, H. C. Hazlett, R. G. Smith, S. Ho, J. C. Gee and G. Gerig, "User-guided 3D active contour segmentation of anatomical structures: Significantly improved efficiency and reliability", *NeuroImage* **31** (2006), no. 3, pp. 1116–1128.

[34] V. Caselles, R. Kimmel and G. Sapiro, "Geodesic active contours", *Int. J. Comput. Vis.* **22** (1997), no. 1, pp. 61–79.

[35] O. Balédent, M. C. Henry-Feugeas and I. Idy-Peretti, "Cerebrospinal fluid dynamics and relation with blood flow: a magnetic resonance study with semiautomated cerebrospinal fluid segmentation", *Invest. Radiol.* **36** (2001), no. 7, pp. 368–377.

[36] C. Xu and J. L. Prince, "Snakes, shapes, and gradient vector flow", *IEEE Trans. Image Process.* **7** (1998), no. 3, pp. 359–369.

[37] O. Baledent, C. Gondry-Jouet, M. E. Meyer, G. De Marco, D. Le Gars, M. C. Henry-Feugeas and I. Idy-Peretti, "Relationship between cerebrospinal fluid and blood dynamics in healthy volunteers and patients with communicating hydrocephalus", *Invest. Radiol.* **39** (2004), no. 1, pp. 45–55.

[38] J. R. Womersley, "Oscillatory flow in arteries: the constrained elastic tube as a model of arterial flow and pulse transmission", *Phys. Med. Biol.* **2** (1957), no. 2, article no. 178.

[39] S. Ko, J. Lee, S. Song, D. Kim, S. H. Lee and J.-H. Cho, "Patient-specific hemodynamics of severe carotid artery stenosis before and after endarterectomy examined by 4D flow MRI", *Sci. Rep.* **9** (2019), no. 1, article no. 18554.

[40] M. Ziegler, J. Alfraeus, E. Good, J. Engvall, E. de Muinck and P. Dyverfeldt, "Exploring the relationships between hemodynamic stresses in the carotid arteries", *Front. Cardiovasc. Med.* **7** (2020), article no. 617755.

[41] F. Hölzle, B. Hohlweg-Majert, M. R. Kesting, T. Mücke, D. J. Loeffelbein, K. D. Wolff and A. Wysluch, "Reverse flow facial artery as recipient vessel for perforator flaps", *Microsurgery* **29** (2009), no. 6, pp. 437–442.

[42] M. Cibis, W. V. Potters, M. Selwaness, et al., "Relation between wall shear stress and carotid artery wall thickening MRI versus CFD", *J. Biomech.* **49** (2016), no. 5, pp. 735–741.

[43] I. E. Sanharawi, M. Barral, S. Lenck, et al., “Wall shear stress in the feeding native conduit arteries of superficial arteriovenous malformations of the lower face is a reliable marker of disease progression”, *Ultraschall Med. - Eur. J. Ultrasound* **41** (2020), no. 4, pp. 428–438.

[44] M. Ahmadpour-B, A. Nooraeen, M. Tafazzoli-Shadpour and H. Taghizadeh, “Contribution of atherosclerotic plaque location and severity to the near-wall hemodynamics of the carotid bifurcation: an experimental study and FSI modeling”, *Biomech. Model. Mechanobiol.* **20** (2021), no. 3, pp. 1069–1085.

[45] J. Faurie, M. Baudet, K. C. Assi, D. Auger, G. Gilbert, F. Tournoux and D. Garcia, “Intracardiac vortex dynamics by high-frame-rate Doppler vortography—in vivo comparison with vector flow mapping and 4-D flow MRI”, *IEEE Trans. Ultrason. Ferroelectr. Freq. Control* **64** (2017), no. 2, pp. 424–432.

[46] F. J. Contijoch, M. Horowitz, E. Masutani, S. Kligerman and A. Hsiao, “4D flow vorticity visualization predicts regions of quantitative flow inconsistency for optimal blood flow measurement”, *Radiol. Cardiothorac. Imaging* **2** (2020), no. 1, article no. e190054.

[47] F. Zhang, C. Lanning, L. Mazzaro, et al., “In vitro and preliminary in vivo validation of echo particle image velocimetry in carotid vascular imaging”, *Ultrasound Med. Biol.* **37** (2011), no. 3, pp. 450–464.

[48] J. Jensen, C. A. Villagómez Hoyos, M. S. Traberg, et al., “Accuracy and precision of a plane wave vector flow imaging method in the healthy carotid artery”, *Ultrasound Med. Biol.* **44** (2018), no. 8, pp. 1727–1741.

[49] M. M. Pedersen, M. J. Pihl, P. Haugaard, K. L. Hansen, T. Lange, L. Lönn, M. B. Nielsen and J. A. Jensen, “Novel flow quantification of the carotid bulb and the common carotid artery with vector flow ultrasound”, *Ultrasound Med. Biol.* **40** (2014), no. 11, pp. 2700–2706.

[50] E. A. Kuczynski, P. B. Vermeulen, F. Pezzella, R. S. Kerbel and A. R. Reynolds, “Vessel co-option in cancer”, *Nat. Rev. Clin. Oncol.* **16** (2019), no. 8, pp. 469–493.

[51] E. Latacz, E. Caspani, R. Barnhill, C. Lugassy, C. Verhoef, D. Grünhagen and P. B. Vermeulen, “Pathological features of vessel co-option versus sprouting angiogenesis”, *Angiogenesis* **23** (2020), no. 1, pp. 43–54.

[52] O. Tan, M. Kantarci, D. Parmaksizoglu, U. Uyanik and I. Durur, “Determination of the recipient vessels in the head and neck using multislice spiral computed tomography angiography before free flap surgery: a preliminary study”, *J. Craniofac. Surg.* **18** (2007), no. 6, pp. 1284–1289.

[53] J. Bettoni, G. Pagé, A.-V. Salsac, et al., “Contribution of flow MRI in the therapeutic management of middle face high flow arteriovenous malformation: a case report”, *J. Stomatol. Oral Maxillofac. Surg.* **120** (2019), no. 4, pp. 361–365.

[54] T. K. Truong, L. J. Wang, I. S. Reed and W. S. Hsieh, “Image data compression using cubic convolution spline interpolation”, *IEEE Trans. Image Process.* **9** (2000), no. 11, pp. 1988–1995.

[55] E. Enjilela, T. Y. Lee, G. Wisenberg, P. Teefy, R. Bagur, A. Islam, J. Hsieh and A. So, “Cubic-spline interpolation for sparse-view CT image reconstruction with filtered backprojection in dynamic myocardial perfusion imaging”, *Tomography* **5** (2019), no. 3, pp. 300–307.